

**Project report for SCEC award # 20115:
Resolving finite source attributes of moderate magnitude earthquakes of
the 2019 Ridgecrest earthquake sequence**

Wenyuan Fan (PI) & Haoran Meng (Co-PI)

1 Project Objectives and Summary

The project aims to investigate rupture processes of moderate to small magnitude earthquakes of the 2019 Ridgecrest earthquake sequence and quantify the uncertainties of the obtained source parameters. We are currently working on a manuscript to summarize the project findings. Upon submission, we will upload the data products (source time functions and the second moments models) and the processed waveforms, including all the P- and S-waveforms of the target earthquakes and eGfs that were used for the analysis, to the UCSD Library Digital Collections (library.ucsd.edu/dc) and Zenodo (zenodo.org).

Understanding key kinematic finite source parameters of a large population of earthquakes can provide observational constraints for earthquake physics, fault zone properties, and the conditions of rupture dynamics. The related source parameter, e.g., earthquake stress-drop, relates to near-field ground motion and has practical implications. However, it remains challenging to directly solve the finite-source attributes for moderate and small earthquakes, and rupture processes of such events are traditionally resolved using spectral methods in the frequency domain based on pre-assumed rupture models. In this project, we apply a time-domain approach that makes few assumptions to estimate the second-degree seismic moments of 39 M3.8 to 5.5 earthquakes of the 2019 Ridgecrest sequence. The 39 earthquakes occurred on faults that are both parallel and perpendicular to the strike of the Mw 7.1 mainshock. The second moments can represent earthquake finite-source attributes, including the rupture length, width, duration, and directivity. We also quantify the model uncertainties by perturbing the earthquake depth, rotating the focal mechanism, examining the apparent duration, and jackknife-resampling the stations. These tests show that our second moments method can robustly resolve the earthquake source parameters. Our models suggest that most of these earthquakes ruptured bilaterally with a median rupture-speed of 74% of the local shear-wave speed. On average, the rupture length is 3.6 times longer than the rupture width, and the earthquake duration seems to scale with its magnitude. With the kinematic attributes, we estimate the earthquake stress-drops and

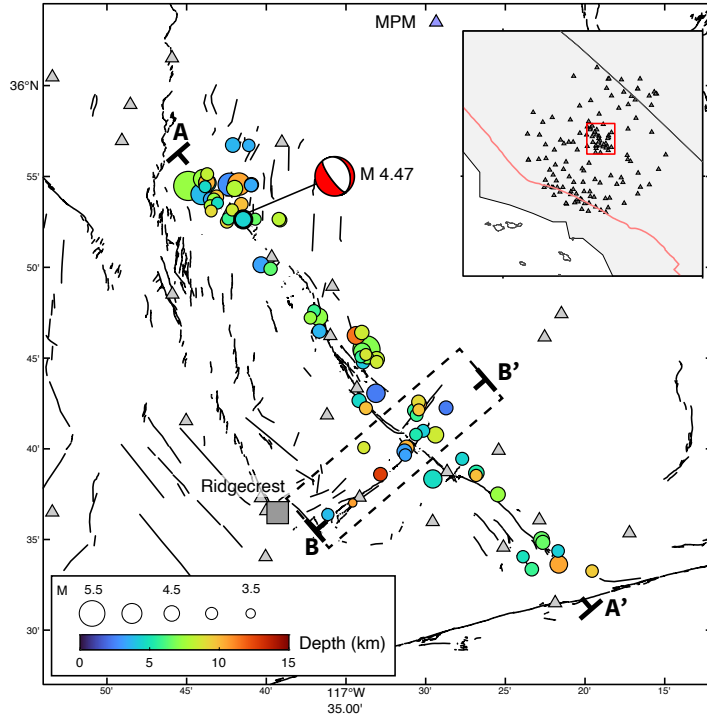


Figure 1: The 2019 Ridgecrest earthquakes and the regional seismic networks (Caltech.Dataset., 2013; Cochran et al., 2020a). The dots are the resolved $3.8 \leq M \leq 5.5$ earthquakes in the region. The triangles are broadband or strong motion stations. The beach ball shows the focal mechanism of an example Mw 4.5 earthquake. The earthquake event ID is 38458079 ($35.8773^\circ / -117.6908^\circ / 4.99$ km). The insert shows all the stations used for the study.

obtained a median stress-drop of 47 MPa. The value is higher than that obtained from spectral analyses. Our stress-drop estimates indicate that these earthquakes likely released a large portion of the total accumulated shear stress of the fault patches.

2 Data and Methods

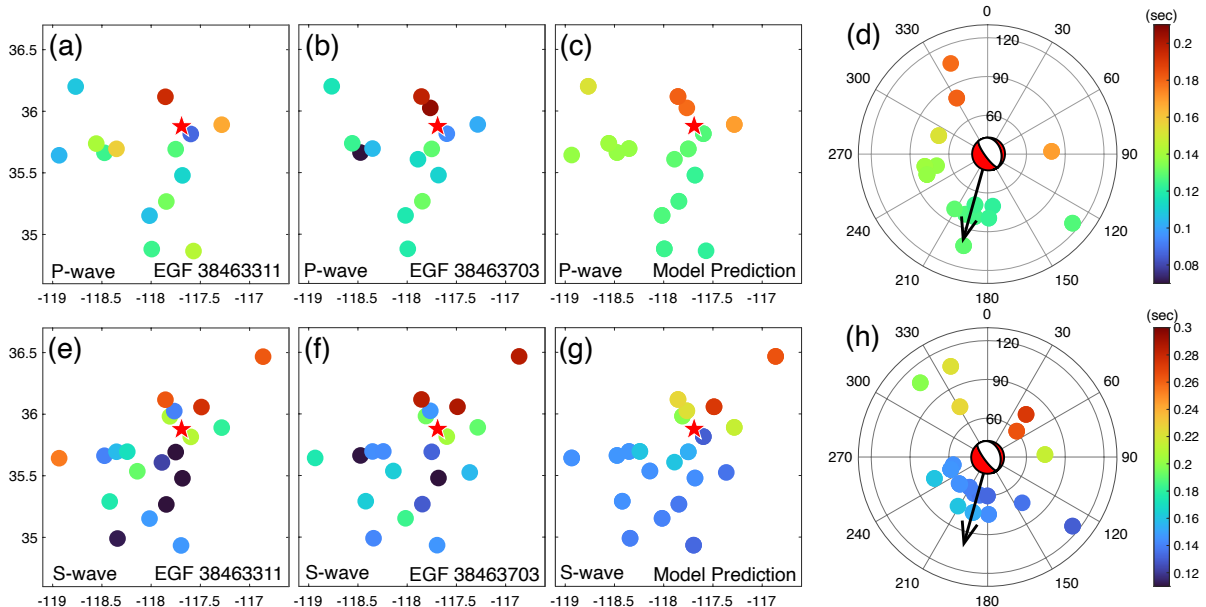


Figure 2: Observed and model predicted apparent durations of an example Mw 4.5 earthquake. (a), observed apparent durations (P-wave) of the earthquake using eGf 38463311. (b), observed apparent durations (P-wave) of the earthquake using eGf 38463703. (c), model-predicted apparent durations for P-wave apparent source time functions (ASTFs). (d) azimuthal view of the measurements with the radius as the take-off angle. (e-h) apparent durations for S-wave ASTFs. legends are similar to (a-d).

2.1 Data

We investigate 81 M3.7 to M5.5 earthquakes of the 2019 Ridgecrest sequence. These events span across the Ridgecrest fault system and the Coso Geothermal Field. We use data from the Southern California Seismic network (Caltech.Dataset., 2013) and campaign networks ZY and GS, which were deployed by the U.S. Geological Survey (Cochran et al., 2020b). Stations with epicentral distances over 120 km are omitted from the second moments analysis. In total, there are over 100 available stations with either broadband (HH channels) or strong motion (HN channels) records. The dense networks provide a relatively uniform azimuthal coverage of the target earthquakes for the second seismic moment analysis (Figure 1).

Using a similar pre-processing procedure in Meng et al. (2020), we obtain 180-second long body wave records with the starting time 10 seconds before the event origin times. First, acceleration records are integrated into velocity records, and all the records are band-pass filtered at 0.5 to 20 Hz using a casual second-order Butterworth filter. The horizontal components are then rotated to the transverse and radial directions to enhance the SH-wave signals. We use the vertical component to model the P-waves. All the filtered records are visually inspected, and the emergent phases and the clipped waveforms are removed.

For the second moments analysis, we also obtain records of small earthquakes as the empirical Green's functions (eGfs). The small earthquakes are selected from a local earthquake catalog (Hutton et al., 2010) with magnitudes 1.5 to 2.5 units smaller than those of the target events, and the eGf earthquakes are within 3 km of the target earthquakes. We apply the same pre-processing

procedure to the eGf records and allow one target event to have multiple eGf records for the same station. With the records of the target earthquake and the eGfs, we use the Projected Land-Weber Deconvolution (PLD) algorithm to obtain apparent source time functions (ASTFs) of all the earthquake-eGf pairs at each station for P- and S-waves, respectively (Bertero et al., 1997; Lanza et al., 1999). With the ASTFs, we further obtain the apparent durations (e.g., Figure 2), which are used to invert for the second seismic moments.

2.2 Second Seismic Moments

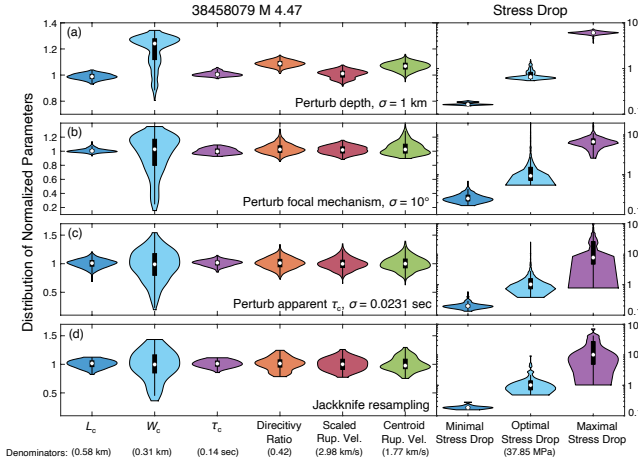


Figure 3: Uncertainty analysis of the example Mw 4.5 earthquake. (a), source parameter distributions when perturbing earthquake depth with a standard deviation (SD) of 1 km (violin plot). Source parameters include the characteristic rupture length L_c , width W_c , duration τ_c , directivity ratio, scaled rupture velocity, centroid rupture velocity, stress drop, and the corresponding lower and upper bounds estimates using minimal and maximal rupture areas. Each parameter is normalized by its optimal solution, which is listed at the bottom of the figure. The stress drop estimates are shown in logarithmic scales, and they are normalized by one value (the preferred solution). (b-d) source parameter distributions by perturbing focal mechanism for an SD of 10° for both strike and dip, apparent τ_c for an SD of 0.0231 seconds (mean residual), and jackknife-resampling of the stations. The legends are similar to those of (a).

characteristic rupture extents ($x_c(\hat{n}) = 2\sqrt{\hat{n}^T \hat{\mu}^{(2,0)} \hat{n}}$), where \hat{n} is a unit eigenvector of $\hat{\mu}^{(2,0)}$ and x_c represents the associated rupture dimension. The characteristic length L_c , width W_c are the first and second largest eigenvalues of $x_c(\hat{n})$, respectively (McGuire, 2004). In addition, we can obtain the apparent rupture velocity ($v_c = L_c/\tau_c$), and centroid rupture velocity $v_0 = \hat{\mu}^{(1,1)}/\hat{\mu}^{(0,2)}$ for a target earthquake. From the apparent and the centroid rupture velocities, we can compute a directivity ratio ($dir = \frac{|v_0|}{v_c}$) for the earthquake, which ranges from 0 to 1. For a perfectly symmetric bilateral rupture, the directivity ratio is 0, and it is 1 for a unilateral rupture propagation. To obtain a physically meaningful rupture velocity, we scale the apparent rupture velocity v_c by a factor of $(1 + dir)/2$ to approximate a realistic rupture velocity, which can characterize a rupture front for both bilateral and unilateral bilateral rupture cases.

With the apparent durations and a local 1D velocity model, we can solve the second moments for the target earthquakes (Meng et al., 2020; Fan and McGuire, 2018; McGuire, 2004, 2017). In this study, we obtain a 1D velocity model from averaging the community velocity model of Southern California (Lee et al., 2014). Centroid location and centroid time are the first moments of an earthquake, and the second seismic moments characterize the variances of the first moments. Therefore, the second moments can represent earthquake length, width, duration and rupture directivity (Backus and Mulcahy, 1976a,b; McGuire, 2004). The second seismic moments $\hat{\mu}^{(2,0)}$, $\hat{\mu}^{(0,2)}$, and $\hat{\mu}^{(1,1)}$ can be inverted from:

$$\hat{\mu}^{(0,2)}(\underline{s}) = \hat{\mu}^{(0,2)} - 2\underline{s} \cdot \hat{\mu}^{(1,1)} + \underline{s} \cdot \hat{\mu}^{(2,0)} \underline{s}$$

where $\hat{\mu}^{(0,2)}(\underline{s})$ is the apparent duration obtained from the ASTF and \underline{s} is the slowness of either P- or S-waves in the source region for a given source-receiver pair (McGuire, 2004). The second moments can estimate an earthquake characteristic duration ($\tau_c = 2\sqrt{\hat{\mu}^{(0,2)}}$) and earthquake

2.3 Source Parameter Uncertainty Analysis

We evaluate the source parameter uncertainties, in particular the rupture area (stress-drop), due to both the model assumptions and the data errors. For the model assumption induced uncertainty, we determine the upper and lower bounds on rupture area that are permissible for a given data set (McGuire and Kaneko, 2018). This exercise determines the intrinsic trade-offs among the second moments given they are not all independent (McGuire and Kaneko, 2018). In this study, we evaluate the extreme models that are permitted the dataset by constraining the data misfit within the 95% confidence interval based on the χ^2 statistic. Assuming the average variance of the data misfit is σ^2 and the degrees of freedom is $N - 3$ where N is the total number of measurements, we aim to solve for the permissible models with the maximum and minimum areas, which predictions are within the maximum permissible misfit, $\sigma^2 \cdot \chi_{95\%, N-3}^2$.

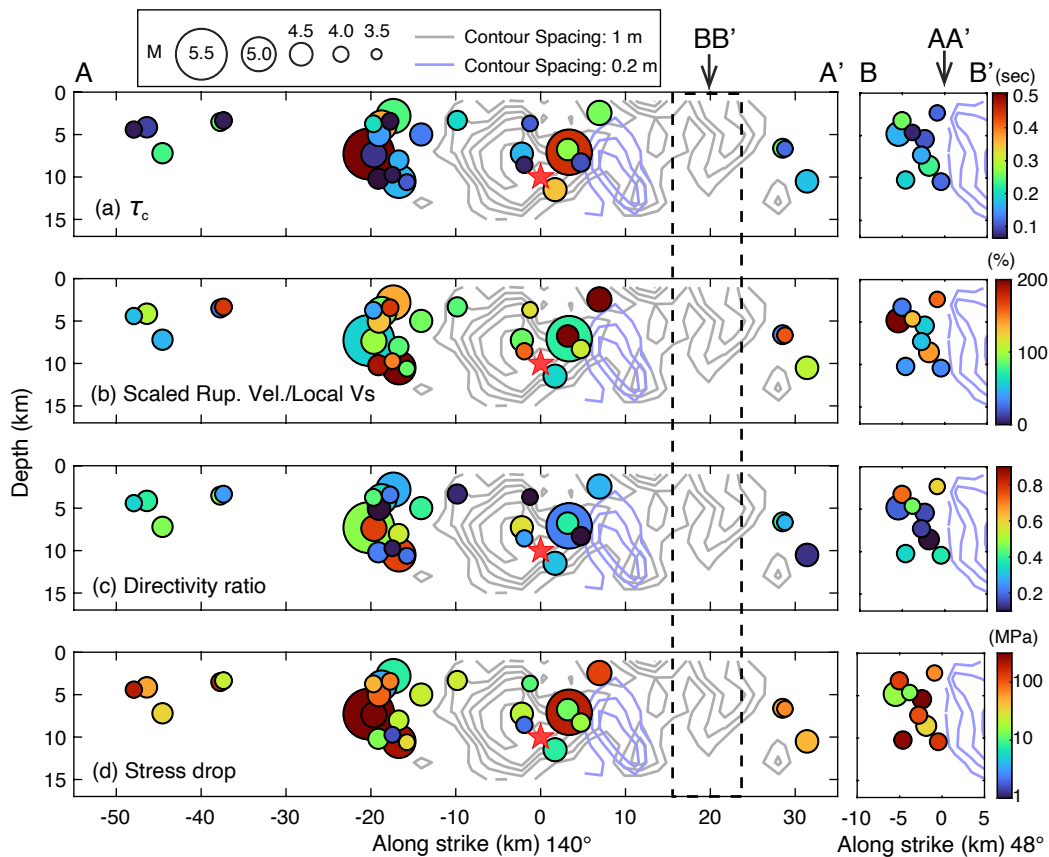


Figure 4: Finite source attributes of 39 M3.8 to M5.5 Ridgecrest earthquakes. (a), characteristic durations of earthquakes along profile AA' showing in Figure 1. Earthquake magnitude scales with the circle size. The grey and light blue contours show the slip distribution of the Mw 7.1 mainshock and the Mw 6.4 foreshock of the 2019 Ridgecrest earthquake sequence, respectively (Jia et al., 2020). (b-d), ratio of the scaled rupture velocity and the local shear velocity (b), directivity ratio (c), and stress drop estimates (d) for earthquakes along profile AA'. (e-h) similar to (a-d) but along profile BB' (Figure 1).

For the data uncertainty-induced source-parameter variability, we examine the influences of the earthquake depth, focal-mechanism, apparent duration, and station distribution. We first consider possible earthquake depth uncertainty by generating a set of 1,000 hypocentral depths of the target earthquake by drawing the depths from a Gaussian distribution with the catalog depth as the mean and a standard deviation of 1 km. For each depth realization, we fix other parameters and perform the same inversion to obtain a second moments model to get a set of finite-source

attributes of the earthquake. Combining source parameters from all the hypocentral depth realizations, we can generate distributions for each kinematic parameter and the stress-drop estimates, including the estimates of the maximum/minimum rupture areas. For example, Figure 3a shows the source parameter variations due to possible depth errors for the example M_w 4.5 earthquake. The results show that the source parameters are insensitive to the earthquake depth uncertainty except for the rupture width (W_c). Similarly, we examine the influences of the focal mechanism uncertainty by using a 2D Gaussian distribution with the earthquake strike and dip as random variables. The distribution has the catalog strike and dip as means and a standard deviation of 10° for each random variable. The obtained source-parameter distributions are similar to those due to depth errors (Figure 3b). To evaluate the effects of the apparent source duration uncertainty, we calculate the differences between the observed and model-predicted durations and then take the mean of the difference as the average standard deviation for all the measured durations. For each duration, we generate a Gaussian distribution with the measured value as the mean and the average standard deviation to draw realizations. The duration draws are independent for different stations. For the example M_w 4.5 earthquake, the standard deviation of the duration is 0.0231 second. Finally, we evaluate the station distribution influences by performing jackknife resampling to the 68 measured τ_c (s) for the M_w 4.5 earthquake. The jackknife resampling results are summarized in Figure 3d. These data uncertainties, including the event depth, focal-mechanism, apparent duration, and the station distribution, mostly affect the characteristic width W_c , while the rest of the parameters are less sensitive to the perturbations. The variation of width W_c casts impacts on the stress-drop estimates. However, the deviations (a few times) are smaller than typical stress-drop estimates (a few orders of magnitude). The upper bound of stress-drop estimate is strongly affected by the uncertainties, showing the minimum rupture area is difficult to constrain.

3 Finite-source attributes of 39 M3.8 to M5.5 Ridgecrest earthquakes

Thirty-nine of the 81 $3.5 \leq M \leq 5.5$ Ridgecrest earthquakes can be reliably resolved (Figure 1,4). Most of the 39 earthquakes occurred outside of the large slip areas of the M_w 6.4 foreshock and the M_w 7.1 mainshock, and some of the earthquakes occurred near the Coso Geothermal Field (Figure 1,4). The duration of the earthquakes lasts from 0.1 to 0.5 seconds, and the duration scales with the earthquake magnitude (Figure 4a). The scaled rupture velocity has a median of 74% of the local S-wave velocity (Figure 4b), confirming the assumed rupture velocity used in most spectral analyses (80% of local S-wave velocity). However, the 39 earthquakes ruptured at a wide range of velocities with several events apparently rupturing at supershear speeds. This is likely due to the poor constrain of the rupture width W_c (Figure 3) as we do not observe supershear rupture speeds along the fault strike. The resolved slip models show a variety of directivity towards all directions. This shows differences between the Ridgecrest faults and other southern California faults, which earthquakes seem to preferably slip along the fault strikes (Meng et al., 2020). Overall, the earthquake directivity ratio ranges from 0.1 to 0.8 with a median of 0.342, suggesting most of the earthquakes likely ruptured bilaterally instead of unilaterally (Figure 4c).

With the estimated rupture dimension (L_c and W_c) and the earthquake moment magnitude, we obtain the earthquake stress-drop estimate assuming an elliptical crack with L_c and W_c representing the major and minor radii respectively (Figure 4d). The stress-drop estimates span 3 orders of magnitude from 1 to 670 MPa. The median stress-drop estimate of the earthquakes is 47.4 MPa. Following similar uncertainty analyses (e.g. Figure 3), we confirm that the stress-drop estimates are robustly constrained. The 47.4 MPa median value is one order higher than that obtained from spectral analyses (Trugman, 2020). Our stress-drop estimates indicate that these earthquakes likely released a large portion of the total accumulated shear stress of the fault patches (Fialko, 2021).

References Cited

- Backus, G. and M. Mulcahy, 1976a: Moment tensors and other phenomenological descriptions of seismic sources-i. continuous displacements. *Geophysical Journal International*, **46** (2), 341–361.
- Backus, G. and M. Mulcahy, 1976b: Moment tensors and other phenomenological descriptions of seismic sources-ii. discontinuous displacements. *Geophysical Journal International*, **47** (2), 301–329.
- Bertero, M., D. Bindi, P. Boccacci, M. Cattaneo, C. Eva, and V. Lanza, 1997: Application of the projected landweber method to the estimation of the source time function in seismology. *Inverse Problems*, **13** (2), 465.
- Caltech.Dataset., 2013: Southern California Earthquake Data Center. doi:10.7909/C3WD3xH1.
- Cochran, E. S., E. Wolin, D. E. McNamara, A. Yong, D. Wilson, M. Alvarez, N. van der Elst, A. McClain, and J. Steidl, 2020a: The U.S. Geological Survey’s rapid seismic array deployment for the 2019 Ridgecrest Earthquake Sequence. *Seismological Research Letters*, **91** (4), 1952–1960, doi: 10.1785/0220190296.
- Cochran, E. S., E. Wolin, D. E. McNamara, A. Yong, D. Wilson, M. Alvarez, N. Van Der Elst, A. McClain, and J. Steidl, 2020b: The us geological survey’s rapid seismic array deployment for the 2019 ridgecrest earthquake sequence. *Seismological Research Letters*, **91** (4), 1952–1960.
- Fan, W. and J. J. McGuire, 2018: Investigating microearthquake finite source attributes with iris community wavefield demonstration experiment in oklahoma. *Geophysical Journal International*, **214** (2), 1072–1087.
- Fialko, Y., 2021: Estimation of absolute stress in the hypocentral region of the 2019 Ridgecrest, California, earthquakes.
- Hutton, K., J. Woessner, and E. Hauksson, 2010: Earthquake monitoring in southern california for seventy-seven years (1932–2008). *Bulletin of the Seismological Society of America*, **100** (2), 423–446.
- Jia, Z., X. Wang, and Z. Zhan, 2020: Multifault models of the 2019 ridgecrest sequence highlight complementary slip and fault junction instability. *Geophysical Research Letters*, **47** (17), e2020GL089802.
- Lanza, V., D. Spallarossa, M. Cattaneo, D. Bindi, and P. Augliera, 1999: Source parameters of small events using constrained deconvolution with empirical green’s functions. *Geophysical journal international*, **137** (3), 651–662.
- Lee, E.-J., P. Chen, T. H. Jordan, P. B. Maechling, M. A. Denolle, and G. C. Beroza, 2014: Full-3-D tomography for crustal structure in southern California based on the scattering-integral and the adjoint-wavefield methods. *Journal of Geophysical Research: Solid Earth*, **119** (8), 6421–6451.
- McGuire, J. J., 2004: Estimating finite source properties of small earthquake ruptures. *Bulletin of the Seismological Society of America*, **94** (2), 377–393, doi:10.1785/0120030091.
- McGuire, J. J., 2017: A MATLAB toolbox for estimating the second moments of earthquake ruptures. *Seismological Research Letters*, **88** (2A), 371–378, doi:10.1785/0220160170.

- McGuire, J. J. and Y. Kaneko, 2018: Directly estimating earthquake rupture area using second moments to reduce the uncertainty in stress drop. *Geophysical Journal International*, **214** (3), 2224–2235.
- Meng, H., J. J. McGuire, and Y. Ben-Zion, 2020: Semiautomated estimates of directivity and related source properties of small to moderate southern california earthquakes using second seismic moments. *Journal of Geophysical Research: Solid Earth*, **125** (4), e2019JB018566.
- Trugman, D. T., 2020: Stress-drop and source scaling of the 2019 ridgecrest, california, earthquake sequence. *Bulletin of the Seismological Society of America*, **110** (4), 1859–1871.